Macroscale transport in channel-matrix systems via integral transforms

B. Ling [1,2] C. B. Rizzo [3] I. Battiato[2] and F. P. J. de Barros [3]

[1]*Institute of Mechanics, Chinese Academy of Sciences, Beijing 100190, China*
[2]*Department of Energy Resources Engineering, Stanford University, Stanford, California 94305, USA*
[3]*Sonny Astani Department of Civil and Environmental Engineering, University of Southern California, Los Angeles, California 90089, USA*

Flow and transport in coupled channel-matrix systems are ubiquitous to many environmental and engineering applications such as flows in fractured porous media over canopies and in membrane filtration units. The multiscale nature of such systems, where the horizontal length scale is often orders of magnitude larger than the vertical one, allows one to employ vertically averaged descriptions of the system. As a result, two-dimensional transport in the channel and the matrix can be upscaled to a coupled system of transient one-dimensional advection-dispersion equations, where matrix and channel properties can be analytically related to macroscopic transport observables. In this work, we first develop a semianalytical solution based on integral transforms that can be employed to predict macroscopic transport in channel-matrix shear flows in a computationally efficient manner. Then we demonstrate that under appropriate dynamic conditions, the coupled system at the macroscale can be further simplified to a single upscaled one-dimensional advection-dispersion equation, which admits an analytical closed-form solution, thus enabling real-time macroscale concentration estimates in relevant applications.

I. INTRODUCTION

Flows above surfaces with complex topological features or coated by porous media, often referred to as channel-matrix systems [1–3] and/or obstructed shear flows [4,5], are present in many environmental, biological, and engineering applications at virtually any scale. Such textured surfaces constitute the physical boundaries that regulate and control mass, momentum and energy fluxes between adjacent systems. Some examples include surfaces of channels and pores in geological formations and hydraulically fractured rocks [6,7]; the surfaces of flowers, leaves, and roots [8–10]; carbon nanotube coatings in shear sensors, ultracapacitors and batteries [11]; canopy-coated riverbeds [12–15]; and coral reefs and urban canopies [16,17].

Textured and porous surfaces exhibit macroscopic properties and dynamical responses to external stimuli that can significantly deviate from the behavior of their smooth counterparts'. For example, micropatterns can lead to drag reduction and/or enhanced scalar mixing in both laminar and turbulent flows [14,18–24]; they can alter the surface wettability or impact fouling propensity in reverse osmosis membranes [25–27]. A number of novel technologies make use of ultraporous coatings to increase, for example, the heat exchange and capacitance in energy storage devices [28,29].

A common feature among most of these systems is the presence of shear as a consequence of the interaction of a free flow with a textured permeable/porous surface. The primary challenge in modeling such systems, and specifically their macroscopic response, lies in their inherent multiscale nature: The characteristic size of the surface features or the porous medium can be orders of

magnitude smaller than the largest scales of the system. Despite the relative lack of understanding of the connection between microscopic parameters and macroscopic properties, i.e., between structure and function, the multiscale nature of the problem renders numerical investigations particularly challenging. However, porous media theory, where the matrix can be treated as a continuum, have been successfully employed to model laminar and turbulent flows over different types of textured surfaces characterized by both ordered or disordered arrays of obstacles at different scales, while they provide a framework to relate macroscale response (e.g., effective slip, dispersion coefficients) to the properties of the effective medium (e.g., permeability) [13,20]. Ling *et al.* [30] have shown experimentally and computationally that a continuum approximation may still be appropriate even for a few layers of obstacles constituting the matrix. Porous media theory has been applied to model flow over and within microscale riblets in superhydrophobic surfaces [31] and carbon nanotube forests [32], in microfluidic mixers [30], in biological [33,34] and membrane filtration systems [25,26,35], and through submerged canopy layers [13–15]. Through the use of integral transforms, Rubol *et al.* [14] derived a semianalytical solution for the advection-dispersion equation in a obstructed shear flow (i.e., aquatic flows over submerged vegetation) and showed how the permeability of the obstruction affected solute mass fluxes and peak concentrations. Ling *et al.* [36] numerically solved transport in a channel-matrix system in the presence of advection and anisotropic dispersion in the permeable media.

Further *ad hoc* approximations—which reduce the problem dimensionality from two-dimensional (2D) to 1D—can be made if, e.g., transport in the matrix is purely diffusive (i.e., matrix permeability is very low) or transport in the matrix is advection dominated (i.e., matrix permeability is high) and the horizontal length is much larger than the overall height of the channel-matrix system. In the former case, Tang *et al.* [6] developed analytical solutions in a one-dimensional channel embedded in an impermeable (to flow) porous matrix. More recently, other works [37,38] developed an analytical or semianalytical model that couples nonuniform channel (or fracture) velocity and diffusion-driven matrix transport. The model of Dejam *et al.* [37] shows good applicability in tight matrix systems and has been extended to reactive transport [39,40]. In the latter case, the system can be further upscaled/averaged in the vertical direction and described by a system of two coupled one-dimensional partial differential equations (PDEs) as derived and analyzed in Refs. [30,36]. Note that matrix permeability effects may not always be neglected, especially in applications where dispersive effects are important such as in geothermal energy production [41] and in natural aquatic systems [42–44].

In this work, we consider flow in a planar channel embedded in a permeable porous matrix. This configuration mimics relevant environmental shear flow systems such as channel-porous matrix [6,7,45] or river flow with surrounding permeable media (i.e., vegetation, riparian area) [14,46–48]. Starting from the model of Ling *et al.* [36], we develop a new semianalytical solution for the coupled system of 1D macroscopic advection-dispersion equations based on the generalized integral transform technique (GITT) [49,50]. The solution is applicable to a much more general class of problems, whose balance laws have a given form. A comparison between the approximate 1D GITT solutions, the numerical solution of the 1D coupled macroscopic PDEs and the spatially averaged 2D microscale equations is provided, together with a convergence and error analysis. Furthermore, we show that, under appropriate dynamic conditions, controlled by the magnitude of the Peclét number (Pe), the system can be further simplified to a 1D PDE which admits a closed-form solution for the average concentration in the channel and the matrix.

II. THEORY

A. Problem formulation

The problem of interest consists of two domains: a porous medium and a channel embedded in it. Both domains are saturated by an incompressible fluid, with a passive solute dissolved in it. We consider a fully developed (unidirectional) flow in the 2D domain depicted in Fig. 1. The Cartesian
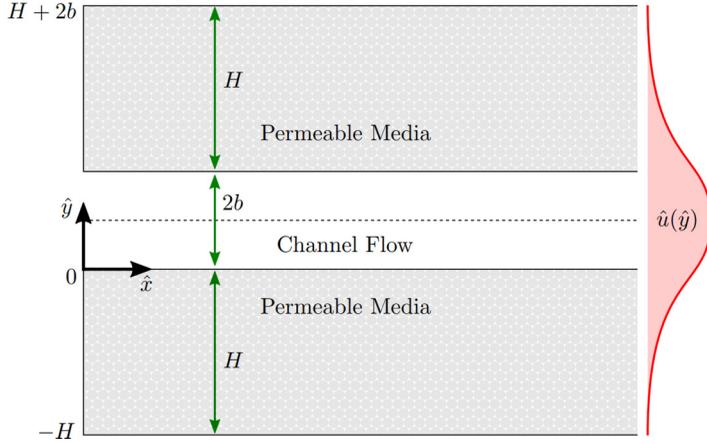
FIG. 1. Problem domain and coordinate system.

coordinate system is denoted by $(\hat{x}, \hat{y})$. The semi-infinite channel of width $2b$ is embedded in a porous material characterized by an effective porosity ϕ, permeability κ and transverse dimension H. The longitudinal velocity in the channel or porous medium is represented by $\hat{u}_i$ with $i = 1$ denoting the channel and $i = 2$ denoting the porous matrix. In our work, the fully developed flow in the channel-porous matrix system is described by coupling Stokes equation (within the channel) and Darcy-Brinkman model (for the permeable medium) [2,13,36]

$$\mu \frac{d^2 \hat{u}_1(\hat{y})}{d\hat{y}^2} - \mathcal{J} = 0 \ \text{ for } \ \hat{y} \in (0, b), \tag{1}$$

$$\mu \frac{d^2 \hat{u}_2(\hat{y})}{d\hat{y}^2} - \frac{\mu}{\kappa} \hat{u}_2(\hat{y}) - \mathcal{J} = 0 \ \text{ for } \ \hat{y} \in (-H, 0), \tag{2}$$

where $\mathcal{J} \equiv d\hat{p}/d\hat{x}$ is the constant pressure gradient and μ is the dynamic viscosity of the fluid. The boundary conditions are as follows:

$$\hat{u}_2(\hat{y})|_{\hat{y}=-H} = 0; \quad \left.\frac{d\hat{u}_1(\hat{y})}{d\hat{y}}\right|_{\hat{y}=b} = 0; \quad \left.\frac{d\hat{u}_1(\hat{y})}{d\hat{y}}\right|_{\hat{y}=0} = \left.\frac{d\hat{u}_2(\hat{y})}{d\hat{y}}\right|_{\hat{y}=0}; \quad \hat{u}_1(\hat{y})|_{\hat{y}=0} = \hat{u}_2(\hat{y})|_{\hat{y}=0}. \tag{3}$$

An inert scalar is continuously released into the channel-matrix system. Transport in the obstructed shear flow is assumed to be governed by a coupled system of advection-diffusion and advection-dispersion equations

$$\frac{\partial \hat{c}_1(\hat{x}, \hat{y}, \hat{t})}{\partial \hat{t}} + \hat{u}_1(\hat{y})\frac{\partial \hat{c}_1(\hat{x}, \hat{y}, \hat{t})}{\partial \hat{x}} = \hat{D}_1 \frac{\partial^2 \hat{c}_1(\hat{x}, \hat{y}, \hat{t})}{\partial \hat{x}^2} + \hat{D}_1 \frac{\partial^2 \hat{c}_1(\hat{x}, \hat{y}, \hat{t})}{\partial \hat{y}^2} \quad \text{for } \hat{y} \in (0, b), \tag{4}$$

$$\frac{\partial \hat{c}_2(\hat{x}, \hat{y}, \hat{t})}{\partial \hat{t}} + \hat{u}_2(\hat{y})\frac{\partial \hat{c}_2(\hat{x}, \hat{y}, \hat{t})}{\partial \hat{x}} = \hat{D}_{2,x} \frac{\partial^2 \hat{c}_2(\hat{x}, \hat{y}, \hat{t})}{\partial \hat{x}^2} + \hat{D}_{2,y} \frac{\partial^2 \hat{c}_2(\hat{x}, \hat{y}, \hat{t})}{\partial \hat{y}^2} \quad \text{for } \hat{y} \in (-H, 0), \tag{5}$$

with $\hat{c}_i$ representing the concentration in the channel ($i = 1$) and permeable medium ($i = 2$). The molecular diffusion coefficient in the channel is given by $\hat{D}_1$. The anisotropic diffusion coefficients in the porous medium domain are defined as $\hat{D}_{2,x}$ and $\hat{D}_{2,y}$, and all the diffusion coefficients are constant in this study. For varying diffusion coefficients, i.e., when non-Fickian transport at small scale [51] and/or continuum scale dispersion due to the local velocity heterogeneity occur, the same

upscaling process as presented in this study can be adopted. The initial and boundary conditions for the transport problem are given by

$$\hat{c}_1(\hat{x}, \hat{y}, 0) = 0; \quad \hat{c}_2(\hat{x}, \hat{y}, 0) = 0, \tag{6}$$

$$\hat{c}_1(0, \hat{y}, \hat{t}) = c_o \ \text{ for } \ \hat{y} \in (0, b); \quad \hat{c}_1(\infty, \hat{y}, \hat{t}) = 0 \ \text{ for } \ \hat{y} \in (0, b); \quad \left.\frac{\partial \hat{c}_1(\hat{x}, \hat{y}, \hat{t})}{\partial \hat{y}}\right|_{\hat{y}=b} = 0, \tag{7}$$

$$\left.\frac{\partial \hat{c}_2}{\partial \hat{x}}\right|_{\hat{x}=0} = 0 \ \text{ for } \ \hat{y} \in (-H, 0); \quad \hat{c}_2(\infty, \hat{y}, \hat{t}) = 0 \ \text{ for } \ \hat{y} \in (-H, 0); \quad \left.\frac{\partial \hat{c}_2(\hat{x}, \hat{y}, \hat{t})}{\partial \hat{y}}\right|_{\hat{y}=-H} = 0. \tag{8}$$

The injected concentration is given by c_o. No-flux boundary condition is imposed on the wall of the porous layer and symmetric boundary condition is applied at the center of the fracture. The continuity on the channel-matrix interface is imposed through the following conditions:

$$\hat{c}_1(\hat{x}, 0, \hat{t}) = \hat{c}_2(\hat{x}, 0, \hat{t}) \ \text{ and } \ \left.\frac{\partial \hat{c}_1(\hat{x}, \hat{y}, \hat{t})}{\partial \hat{y}}\right|_{\hat{y}=0} = \phi \frac{\hat{D}_{2,y}}{\hat{D}_1} \left.\frac{\partial \hat{c}_2(\hat{x}, \hat{y}, \hat{t})}{\partial \hat{y}}\right|_{\hat{y}=0}. \tag{9}$$

Note that (4) and (5) consider advection and diffusive mass transfer (in $\hat{x}$ and $\hat{y}$ directions) in both the channel and the permeable matrix. This differs from previous models [6,7,38,45,52] where advection in the porous matrix is neglected as well as longitudinal mass exchange.

Next, we define the following dimensionless quantities:

$$x = \frac{\hat{x}}{L}, \quad y = \frac{\hat{y}}{b}, \quad p = \frac{\hat{p}}{p_0}, \quad u_i = \frac{\hat{u}_i}{U} \quad c_i = \frac{\hat{c}_i}{c_o} \quad \text{with} \quad i = \{1, 2\}, \tag{10}$$

where L is a characteristic macroscopic/observation length scale, e.g., the distance far from the inlet where model predictions are registered, p_0 is a characteristic pressure, e.g., the ambient pressure, and U is the average velocity across the channel. Therefore, the dimensionless representation of Eqs. (1) and (2) is

$$\frac{d^2 u_1(y)}{dy^2} - \Psi = 0, \quad y \in (0, 1), \tag{11a}$$

$$\frac{d^2 u_2(y)}{dy^2} - \lambda^2 u_2(y) - \Psi = 0, \quad y \in (-h, 0), \tag{11b}$$

subject to

$$u_2(y)|_{y=-h} = 0, \quad \left.\frac{du_1(y)}{dy}\right|_{y=1} = 0, \quad u_1(y)|_{y=0} = u_2(y)|_{y=0}, \quad \left.\frac{du_1(y)}{dy}\right|_{y=0} = \left.\frac{du_2(y)}{dy}\right|_{y=0}, \tag{12}$$

where

$$\lambda^2 = \frac{b^2}{k}, \quad \Psi = \frac{p_0 b^2}{\mu U L} \frac{dp}{dx}, \quad \text{and} \quad h = \frac{H}{b}. \tag{13}$$

The system (11) admits an analytical solution for the velocity profiles in the channel and the matrix, u_1 and u_2, respectively,

$$u_1(y) = \frac{\Psi}{2} y^2 + Ay + B, \quad y \in [0, 1], \tag{14}$$

$$u_2(y) = -\frac{\Psi}{\lambda^2} + Ee^{\lambda y} + Fe^{-\lambda y}, \quad y \in [-h, 0], \tag{15}$$

where the coefficients A, B, E, and F are

$$A = -\Psi, \tag{16a}$$

$$B = -\frac{\Psi}{\lambda^2}(-1 + e^{\Lambda})(-1 + e^{\Lambda} + \lambda + \lambda^{\Lambda})(1 + e^{2\Lambda})^{-1}, \tag{16b}$$

$$E = -\frac{\Psi}{\lambda^2}e^{\Lambda}(-1 + \lambda e^{\Lambda})(1 + e^{2\Lambda})^{-1}, \tag{16c}$$

$$F = -\frac{\Psi}{\lambda^2}(\lambda + e^{\Lambda})(1 + e^{2\Lambda})^{-1}. \tag{16d}$$

The parameter Λ is defined as

$$\Lambda = \lambda h. \tag{17}$$

We remark that Λ exclusively depend on the geometric properties of the system, and it is the ratio between the square root of the permeability ($\sqrt{k}$) and the characteristic length scale (H) of the porous layer. Following the same procedure, the scalar transport Eqs. (4) and (5) are rewritten in dimensionless form as follows:

$$\epsilon \text{Pe}\frac{\partial c_1(x, y, t)}{\partial \hat{t}} + \epsilon \text{Pe}\, u_1 \frac{\partial c_1(x, y, t)}{\partial x} = \epsilon^2 \frac{\partial^2 c_1(x, y, t)}{\partial x^2} + \frac{\partial^2 c_1(x, y, t)}{\partial y^2} \quad \text{for } y \in (0, 1), \tag{18}$$

$$\epsilon \text{Pe}\,\frac{\partial c_2(x, y, t)}{\partial \hat{t}} + \epsilon \text{Pe}\, u_2 \frac{\partial c_2(x, y, t)}{\partial x} = \epsilon^2 D_{2,x} \frac{\partial^2 c_2(x, y, t)}{\partial x^2} + D_{2,y} \frac{\partial^2 c_2(x, y, t)}{\partial y^2} \quad \text{for } y \in (-h, 0), \tag{19}$$

with

$$\epsilon = \frac{b}{L}; \quad \text{Pe} = \frac{Ub}{\hat{D}_1}; \quad D_{2,x} = \frac{\hat{D}_{2,x}}{\hat{D}_1}; \quad D_{2,y} = \frac{\hat{D}_{2,y}}{\hat{D}_1}, \tag{20}$$

where Pe is the Peclét number. The normalized initial and boundary conditions for the transport problem are

$$c_1(0, y, t) = 1 \text{ for } y \in (0, 1); \quad c_1(\infty, y, t) = 0 \text{ for } y \in (0, 1); \quad \left.\frac{\partial c_1(x, y, t)}{\partial y}\right|_{y=1} = 0,$$

$$\left.\frac{\partial c_2(x, y, t)}{\partial x}\right|_{x=0} = 0 \text{ for } y \in (-h, 0); \quad c_2(\infty, y, t) = 0 \text{ for } y \in (-h, 0);$$

$$\left.\frac{\partial c_2(x, y, t)}{\partial y}\right|_{y=-h} = 0, \tag{21}$$

$$c_1(x, 0, t) = c_2(x, 0, t) \text{ and } \left.\frac{\partial c_1(x, y, t)}{\partial y}\right|_{y=0} = \phi D_{2,y} \left.\frac{\partial c_2(x, y, t)}{\partial y}\right|_{y=0}. \tag{22}$$

B. Upscaling

The 2D transport equations (18) and (19) can be transformed into a coupled system of 1D advection dispersion equations (ADEs) through the use of spatial averaging. Following the procedure described in Ref. [36], we define the spatial averaging operator as

$$\langle \cdot \rangle = \frac{1}{\ell} \int_0^{\ell} dy \tag{23}$$

with $\ell = 1$ the channel region and $\ell = -h$ the porous matrix region. For additional details pertaining the upscaling method, we refer to the work of Ling *et al.* [36]. Performing the spatial averaging together with asymptotic homogenization, the upscaled coupled ADE system reads

$$\frac{\partial \langle c_1 \rangle}{\partial t} = A_1 \frac{\partial \langle c_1 \rangle}{\partial x} + A_2 \frac{\partial^2 \langle c_1 \rangle}{\partial x^2} + A_3 \frac{\partial \langle c_2 \rangle}{\partial x} + A_4 \langle c_1 \rangle + A_5 \langle c_2 \rangle, \tag{24}$$

$$\frac{\partial \langle c_2 \rangle}{\partial t} = B_1 \frac{\partial \langle c_2 \rangle}{\partial x} + B_2 \frac{\partial^2 \langle c_2 \rangle}{\partial x^2} + B_3 \frac{\partial \langle c_1 \rangle}{\partial x} + B_4 \langle c_2 \rangle + B_5 \langle c_1 \rangle, \tag{25}$$

where the variables $\langle c_i \rangle (x, t) = \langle c_i (x, y, t) \rangle$. In this paper, we omit (x, t) from the notation for simplicity. Expressions for the coefficients A_1-A_5 and B_1-B_5 are provided in the Appendix. Notice that the coupled system of partial differential equations, see (24) and (25), can be used to analyze scalar transport for a broad spectrum of physical systems. For instance, when the transient term is neglected and $A_2 = A_3 = 0$, Eq. (24) can applied to model the concentration polarization in a reverse osmosis membrane system [53]. When $B_1 = B_2 = B_3 = 0$, Eq. (25) converts to classic dual-porosity model [54]. For the case when $B_1 = B_3 = B_4 = B_5 = 0$, diffusion is the only transport mechanism in the matrix [37]. Equations (24) and (25) can be written in a compact form that follows the summation convention:

$$\frac{\partial \langle c_i \rangle}{\partial t} = \mathcal{L}_{ij} \langle c_j \rangle, \quad \{i, j\} = 1, 2, \tag{26}$$

where $\mathcal{L}_{ij}$ are four differential operators:

$$\mathcal{L}_{11} = A_1 \frac{\partial \cdot}{\partial x} + A_2 \frac{\partial^2 \cdot}{\partial x^2} + A_4, \tag{27}$$

$$\mathcal{L}_{12} = A_3 \frac{\partial \cdot}{\partial x} + A_5, \tag{28}$$

$$\mathcal{L}_{21} = B_3 \frac{\partial \cdot}{\partial x} + B_5, \tag{29}$$

$$\mathcal{L}_{22} = B_1 \frac{\partial \cdot}{\partial x} + B_2 \frac{\partial^2 \cdot}{\partial x^2} + B_4. \tag{30}$$

The boundary and initial conditions are as follows:

$$\langle c_1 \rangle |_{x=0} = 1; \qquad \langle c_1 \rangle |_{x=\infty} = 0; \qquad \langle c_1 \rangle |_{t=0} = 0, \tag{31}$$

$$\frac{\partial \langle c_2 \rangle}{\partial x} \bigg|_{x=0} = 0; \qquad \langle c_2 \rangle |_{x=\infty} = 0; \qquad \langle c_2 \rangle |_{t=0} = 0. \tag{32}$$

The solutions for Eqs. (24) and (25) are valid for $\epsilon \ll 1$ and $\text{Pe} < \epsilon^{-1/2}$. The upscaled equations are obtained by (i) asymptotically expanding the unknown variables (c_1 and c_2) based on ϵ and (ii) solving the ordered equations with matched magnitude of ϵ. The former condition ($\epsilon \ll 1$) ensures the accuracy of the expansion and the latter one ($\text{Pe} < \epsilon^{-1/2}$) regulates that all the terms are kept in certain order when Pe changes. These conditions are proven to be the *sufficient* conditions for the upscaled equations [30], however, *not necessary*. For instance, when the system has a large flow rate, the concentration reaches saturation shortly after the injection started, and the gradient of the concentration approaches zero, thus the gradient term's influence is negligible [e.g., the third term on the right-hand side of Eqs. (24) and (25)] to the accuracy of the final solution even though the Peclét number is large.

C. Effective velocity and dispersion

Prior to solving the transport problem formulated in (24) and (25), we provide a brief analysis of the role of the parameters λ and h on the flow field in both the channel and porous matrix
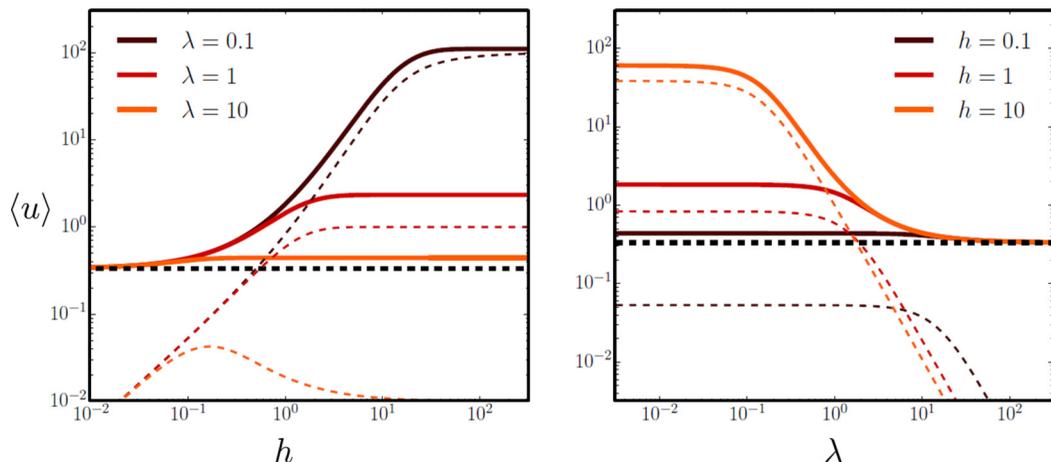
FIG. 2. Average velocities as a function of h and λ. Continuous lines represent the average velocity in the channel $\langle u_1 \rangle$. Dotted lines represent the average velocity in the porous matrix $\langle u_2 \rangle$. The thick black dotted line is the Poiseuille limit $\langle u \rangle = 1/3$.

[see Eqs. (11a) and (11b)] as well as in the upscaled dispersion coefficients, namely A_2 and B_2 [see Eqs. (24) and (25)]. Since transport is affected by the fluid velocity, we show the functional dependence between the average velocity and the parameters λ and h. This analysis will assist in interpreting the computational results.

Mainly we are interested in exploring the average velocity under two limiting cases for λ and h. When h tends to 0, the width of channel becomes large compared to the dimensions of the porous matrix (i.e., $b \gg H$). Under this condition, the channel carries the bulk of the fluid and the system behaves like a channel flow. However, when $\lambda \to \infty$, the permeability in the porous matrix tends to zero and the flow system resembles a channel flow with impermeable walls (i.e., Poiseuille flow). In both limits, the average dimensionless velocity in the channel should asymptotically converge to 1/3, which corresponds to the average velocity in a Poiseuille flow. These results are illustrated in Fig. 2. By fixing λ and varying h, we observe that the average velocity in the channel converges to 1/3 when $h \to 0$ (Fig. 2, left). Figure 2 (right) shows that the average velocity also approaches to 1/3 when we increase λ while keeping h fixed. The average velocity in the porous medium is illustrated in Fig. 2 (see dashed lines), and, as expected, it tends to zero when $\lambda \to \infty$ (Fig. 2, right).

In Eqs. (24) and (25), A_2 and B_2 correspond to the dispersion coefficients. To assess the dispersion coefficients in different geometrical and transport scenarios, we map A_2 and B_2 in a $\mathrm{Pe} - \lambda$ space (Fig. 3). Both A_2 and B_2 are large when $\lambda \to 0$, Additionally, the channel dispersion A_2 shows a dual-peak both at $\mathrm{Pe} \to 0$ and $\mathrm{Pe} \to \infty$. This result is expected: The dispersion coefficient is larger when $\mathrm{Pe} \to 0$, diffusion is the dominant transport mechanism, and when $\mathrm{Pe} \to \infty$ advection plays a major role.

In the following section, we provide a semianalytical solution for (24) and (25).

III. SEMIANALYTICAL SOLUTION VIA INTEGRAL TRANSFORM

A. Transformation

In order to solve the coupled system of 1D ADEs, (24) and (25), we resort to the use of the GITT [49,50,55,56]. This methodology has been adopted to solve scalar transport in channel flow characterized by spatially variable velocity and eddy diffusivities [14,43,57]. It has also been used to address transport in a channel-porous matrix system in the absence of advection in the porous
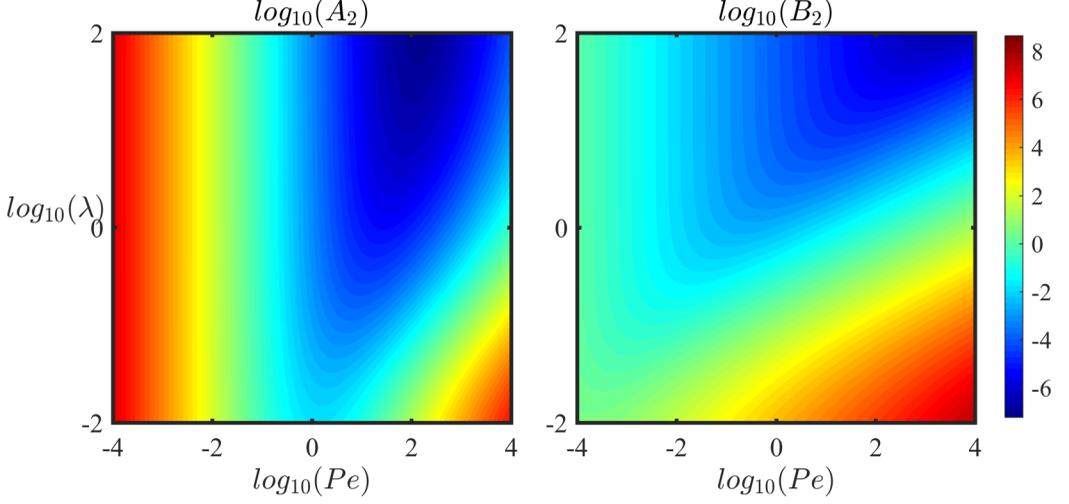
FIG. 3. Behavior of the dispersion coefficients A_2 and B_2 with respect to λ and Pe. The base of the logarithm in the figure is 10.

matrix [52]. In order to apply the GITT, we consider a finite domain $[0, L^*]$, with $L^* \gg L$ where L is the first characteristic length. We start by defining the rescaled variables

$$C_1(x, t) = \langle c_1 \rangle - \left(\frac{L^* - x}{L^*} \right) \quad \text{and} \quad C_2(x, t) = \langle c_2 \rangle. \tag{33}$$

It is worth emphasizing that this transformation ensures the left boundary condition for C_1 becomes homogeneous (i.e., $C_1(0, t) = 0$). We can now rewrite Eqs. (24) and (25) as:

$$\frac{\partial C_i(x, t)}{\partial t} = \mathcal{L}_{ij} C_j(x, t) + C_i^*(x), \quad \{i, j\} = 1, 2, \tag{34}$$

where C_i is an element of $\mathbf{C} = [C_1, C_2]^T$, and C_i^* denotes the additional terms introduced by the transformation, namely:

$$\mathbf{C}^*(x) = [C_1^*(x), C_2^*(x)]^T = \left[-A_1 + A_4 \left(\frac{L^* - x}{L^*} \right), -B_3 + B_5 \left(\frac{L^* - x}{L^*} \right) \right]^T \tag{35}$$

and Eq. (34) is subject to the following initial and boundary conditions:

$$C_1(0, t) = 0, \quad C_1(L^*, t) = 0, \quad C_1(x, 0) = 0, \tag{36a}$$

$$\left. \frac{\partial C_2(x, t)}{\partial x} \right|_{t=0} = 0, \quad C_2(L^*, t) = 0, \quad C_2(x, 0) = 0. \tag{36b}$$

In order to apply the GITT, we define the following integral transform pairs [50,55,56]:

$$\bar{C}_{ki}(t) = \int_0^{L^*} \tilde{\xi}_{ki}(x) C_k(x, t) dx, \quad k = \{1, 2\}, \tag{37}$$

$$C_k(x, t) = \sum_{i=1}^{\infty} \tilde{\xi}_{ki}(x) \bar{C}_{ki}(t), \quad k = \{1, 2\}, \tag{38}$$

where the symmetric kernels $\tilde{\xi}_{ki}(x)$ are defined as follows:

$$\tilde{\xi}_{ki}(x) \equiv \frac{\xi_{ki}(x)}{\sqrt{N_{ki}}}, \quad k = \{1, 2\}. \tag{39}$$

Here N_{ki} corresponds to the norm of the eigenfunctions $\xi_{ki}(x)$. The norm is defined as the integral over the eigenfunction squared over the entire domain [43,52], and it writes:

$$N_{ki} = \int_0^{L^*} \xi_{ki}^2(x)dx. \tag{40}$$

The eigenfunctions are the solution of the uncoupled auxiliary problem,

$$A_2 \frac{d^2\xi_{1i}(x)}{dx^2} + \left(\mu_{1i}^2 + A_4\right)\xi_{1i}(x) = 0, \tag{41}$$

$$B_2 \frac{d^2\xi_{2i}(x)}{dx^2} + \left(\mu_{2i}^2 + B_4\right)\xi_{2i}(x) = 0. \tag{42}$$

Equations (41) and (42) are subject to the following homogeneous boundary conditions:

$$\xi_{1i}(0) = 0; \ \xi_{1i}(L^*) = 0, \tag{43a}$$

$$\left.\frac{d\xi_{2i}(x)}{dx}\right|_{x=0} = 0; \ \xi_{2i}(L^*) = 0. \tag{43b}$$

A set of solutions for Eqs. (41) and (42), satisfying the boundary conditions defined in (43a) and (43b), is

$$\xi_{1i}(x) = \sin(\beta_{1i}x), \tag{44}$$

$$\xi_{2i}(x) = \cos(\beta_{2i}x), \tag{45}$$

where β_{1i} are the positive roots of $\sin(\beta_{1i}L^*) = 0$ and β_{2i} are the positive roots of $\cos(\beta_{2i}L^*) = 0$. Moreover, by using Eqs. (41) and (42), the eigenvalues μ_{ki} are determined by

$$\mu_{1i} = \sqrt{A_2\beta_{1i}^2 - A_4}, \tag{46}$$

$$\mu_{2i} = \sqrt{B_2\beta_{1i}^2 - B_4}. \tag{47}$$

Multiplying Eq. (34) by $\tilde{\xi}_{ki}(x)$, integrating from 0 to L^* and using (37) and (38) together with the boundary conditions, we obtain the following set of coupled ordinary differential equations (for additional details, see Refs. [50,56]):

$$\frac{d\bar{C}_{ki}(t)}{dt} + \mu_{ki}^2\bar{C}_{ki}(t) = \bar{\mathcal{G}}_{ki}(\bar{C}_{1i}(t), \bar{C}_{2i}(t)), \quad k = \{1, 2\}, \tag{48}$$

where the function $\bar{\mathcal{G}}_{ki}(\bar{C}_{1i}, \bar{C}_{2i})$ is written as:

$$\bar{\mathcal{G}}_{1i}(t) = \sum_{j=1}^{\infty} \left\{ \left[-A_1 \int_0^{L^*} \tilde{\xi}_{1i}(x)\frac{d\tilde{\xi}_{1j}(x)}{dx}dx \right]\bar{C}_{1j}(t) + \left[-A_3 \int_0^{L^*} \tilde{\xi}_{1i}(x)\frac{d\tilde{\xi}_{2j}(x)}{dx}dx \right. \right.$$
$$\left. \left. + A_5 \int_0^{L^*} \tilde{\xi}_{1i}(x)\tilde{\xi}_{2j}(x)dx \right]\bar{C}_{2j}(t) \right\} + (A_4 - A_1)\int_0^{L^*} \tilde{\xi}_{1i}(x)dx + \frac{A_4}{L^*}\int_0^{L^*} x\tilde{\xi}_{1i}(x)dx, \tag{49a}$$

$$\bar{\mathcal{G}}_{2i}(t) = \sum_{j=1}^{\infty} \left\{ \left[-B_1 \int_0^{L^*} \tilde{\xi}_{2i}(x)\frac{d\tilde{\xi}_{2j}(x)}{dx}dx \right]\bar{C}_{2j}(t) + \left[-B_3 \int_0^{L^*} \tilde{\xi}_{2i}(x)\frac{d\tilde{\xi}_{1j}(x)}{dx}dx \right. \right.$$
$$\left. \left. + B_5 \int_0^{L^*} \tilde{\xi}_{2i}(x)\tilde{\xi}_{1j}(x)dx \right]\bar{C}_{1j}(t) \right\} + (B_4 - B_1)\int_0^{L^*} \tilde{\xi}_{2i}(x)dx + \frac{B_4}{L^*}\int_0^{L^*} x\tilde{\xi}_{2i}(x)dx. \tag{49b}$$
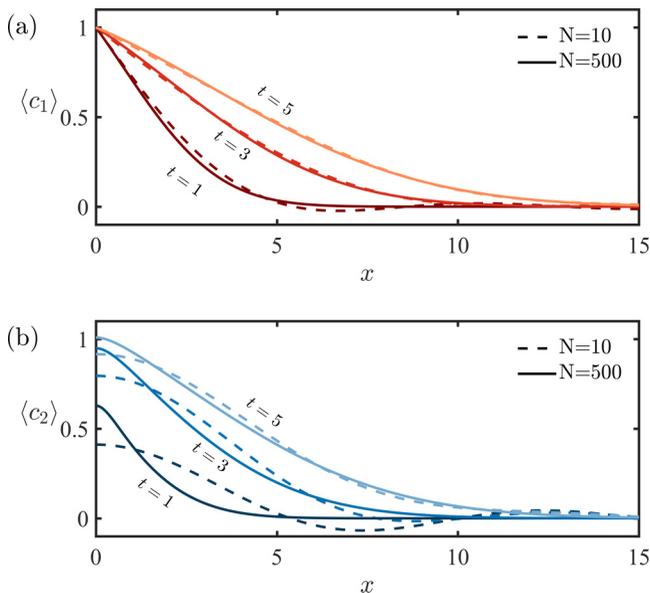
FIG. 4. Eigenfunction convergence analysis of the semianalytical solution obtained with the GITT. (a) $\langle c_1 \rangle$ at different time instance by varying the number of eigenfunctions; (b) $\langle c_2 \rangle$ at different time instance by varying the number of eigenfunctions. Parameter values used to generate the results are associated with scenarios SIM-01 and SIM-05 listed in Table I.

The transformed initial condition is

$$\bar{C}_{1i}(0) = 0, \tag{50a}$$

$$\bar{C}_{2i}(0) = 0. \tag{50b}$$

Note that the integrals involving ξ_{ki} can be computed analytically using any symbolic solver and the system of coupled ordinary differential equations (48) is solved numerically. Once the coefficients $\bar{C}_{ki}$ at any given time step have been determined, the inverse formula (38) is applied to obtain the functions C_1 and C_2 and therefore the concentrations $\langle c_1 \rangle$ and $\langle c_2 \rangle$. To compute the concentration in the channel and the porous matrix, we need to truncate the series expansion, see (38). The truncation order is denoted by N. In the following, we present first a convergence analysis and then investigate the impact of matrix permeability on the scalar concentration distributions.

B. Numerical implementation

We use an implicit Adams scheme to march $\bar{C}_{ki}$ in time, see Eq. (48). The time step used in the scheme is denoted by δt. The GITT algorithm is implemented using the Python language. The simulation parameters (and scenarios) used for all upcoming results are listed in Table I. Next, we perform a convergence study by assessing the truncation error of using N finite terms of the series (38) and temporal accuracy of using time step δt.

Figure 4 shows the result for the computed concentrations using two different N for the channel $\langle c_1 \rangle$ and porous medium $\langle c_2 \rangle$ at distinct times as a function of x. When N is low, the solution has oscillations which can be eliminated by increasing N. Figure 5 illustrates the channel and matrix concentration as a function of the dimensionless time for different dimensionless time steps. The upscaled concentration in both the channel $\langle c_1 \rangle$ and porous medium $\langle c_2 \rangle$ are depicted in Fig. 5 at dimensionless position $x = 1$ and at different dimensionless times ($\delta t = 0.5$, 0.1, and 0.01). To
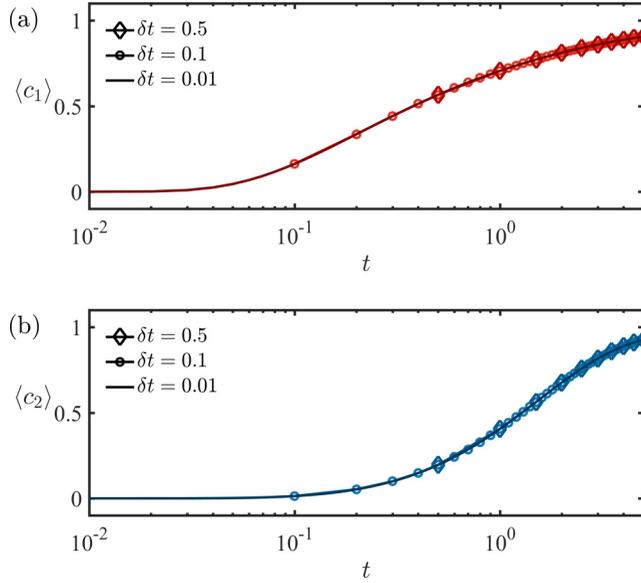
FIG. 5. Time convergence analysis the GITT algorithm. (a) $\langle c_1 \rangle$ at $x = 1$ by varying the time step; (a) $\langle c_2 \rangle$ at $x = 1$ by varying the time step. Simulations parameters are provided in scenarios SIM-05, SIM-14, to SIM-16 listed in Table I.

evaluate the error, we define the square mean error as:

$$\mathcal{E}_x(f_{\mathrm{std}}|f) = \frac{1}{n} \sum_{i=1}^{n} \sqrt{[f(x_i, t^*) - f_{\mathrm{std}}(x_i, t^*)]^2} \tag{51}$$

where $\mathcal{E}_x$ is the mean-square error evaluated at $t = t^*$ and n is the total number or output data points. Note that f represents the function to be evaluated (i.e., concentration). The function f_{std} corresponds to the concentration solution obtained with a higher N or smaller δt.
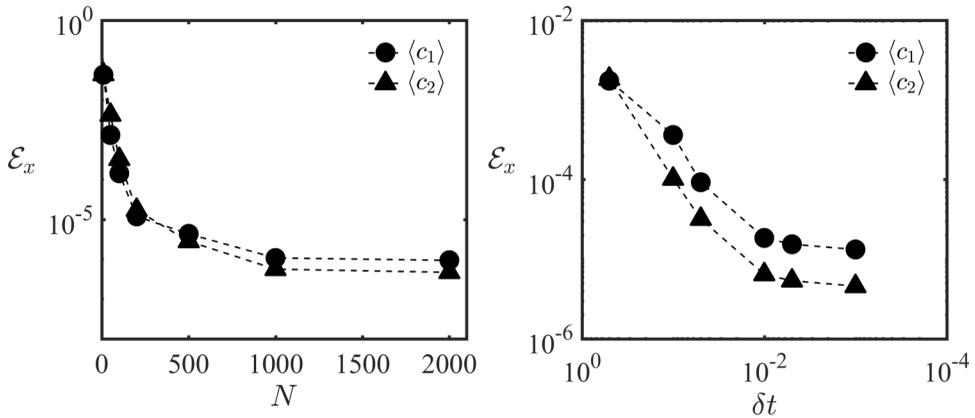

FIG. 6. Analysis of the error $\mathcal{E}_x$ as a function of N and δt. Circle markers correspond to channel results and triangle markers indicate porous matrix solutions. Simulation parameters are SIM-01 to SIM-05, SIM-14 to SIM-16, and SIM-22 to SIM-26 (see Table I).
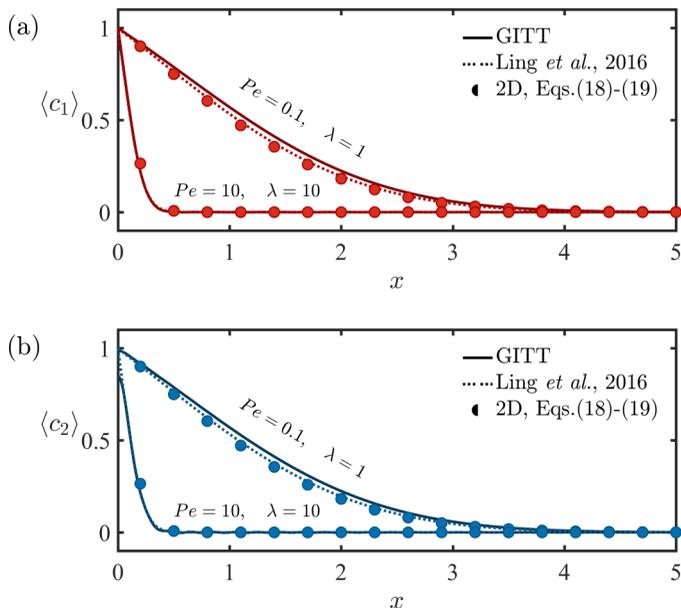
FIG. 7. Comparison between the GITT solution, the solution of (24) and (25) (Ling *et al.* [36]) and the spatial average of the 2D numerical solution of (18) and (19) ("2D") at different dimensionless time $t = 1$. The GITT computational results correspond to the upscaled concentration and the numerical solution refers to the concentration in a 2D system. Results for the concentration in the channel versus distance for $Pe = 10^{-1}$, $\lambda = 1$ and $Pe = 10$, $\lambda = 10$ (see SIM-17 and SIM-18 listed in Table I).

In Fig. 6, we plot the error between the GITT solutions computed with different N, with $N = \{10, 50, 100, 200, 500, 1000, 2000, 5000\}$, and δt, with $\delta t = \{0.1, 0.05, 0.01, 0.005, 0.001\}$. The f_{std} is the solution of a higher N (Fig. 6, left) or a smaller δt (Fig. 6, right). For instance, the error $\mathcal{E}_x$ at $N = 1000$ is computed by using f_{std} at $N = 2000$, and the error at $N = 2000$ is computed by using f_{std} at $N = 5000$. We can see both N and δt show convergent solutions. We consider the solution converged when the error is smaller than 1×10^{-5}. Thus, we conclude that when $N \sim 500$ and $\delta t < 0.1$, the solver converges. All parameters used in the simulations will be listed in Table I.

IV. COMPUTATIONAL RESULTS AND DISCUSSION

We now evaluate the performance of the GITT solution with (i) the numerical solution of the upscaled model presented in Eqs. (24) and (25) (denoted here as "Ling *et al.* [36]") and (ii) the numerical solution of the 2D model presented in Eqs. (18) and (19) (referred as "2D"). For the "Ling *et al.* [36]" solution, Eqs. (24) and (25) were solved by the Matlab's built-in partial differential equation solver PDEPE. As for the "2D" solution, a finite-difference script (i.e., central-difference-backward-time method) was implemented in Matlab to solve Eqs. (18) and (19). Both solvers accuracy and convergence study is performed in Ling *et al.* [36].

The three solutions (GITT, Ling *et al.* and 2D) are plotted in Fig. 7 using the same parameters. Figures 7(a) and 7(b) show the spatial distribution of both the concentration in the channel and porous matrix for $Pe = 10^{-1}$, $\lambda = 1$ and $Pe = 10$, $\lambda = 10$, respectively. As observed in Fig. 7, a good agreement is obtained between the upscaled concentration and the numerical solution of the full 2D system. The results depicted in Fig. 7 also show the capability of the upscaled model, solved using the GITT, in reproducing the concentration field in the original 2D setting.

Figure 8 illustrates the spatial distribution of the upscaled concentration profile in the channel (red lines) and the porous matrix (blue line) for different dimensionless times ($t = 1$ and 5) and $h =$
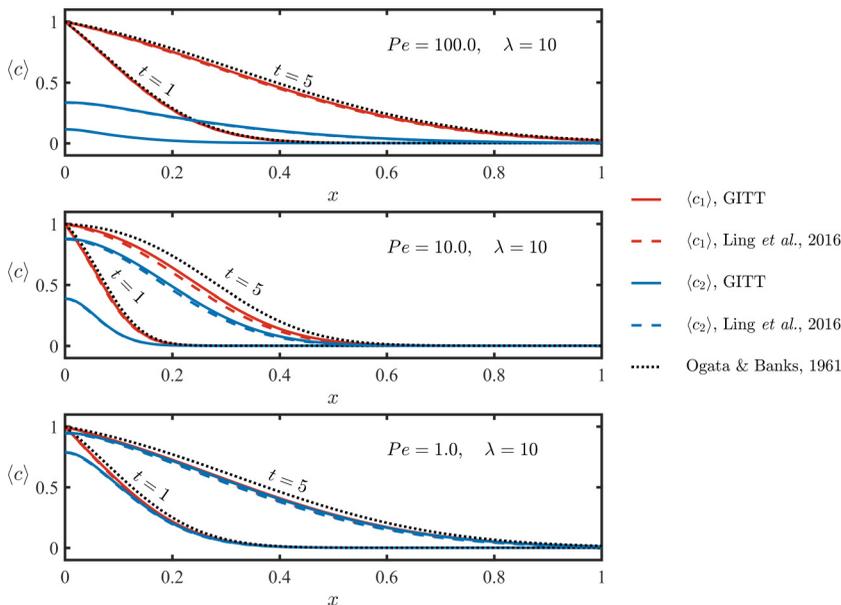
FIG. 8. Comparison between the GITT solution, the numerical solution of (24) and (25) (Ling *et al.* [36]) and the Ogata-Banks solution (53). The red solid line indicates the GITT channel solution ($\langle c_1 \rangle$) and the blue solid line represents matrix solution ($\langle c_2 \rangle$). The red and blue dashed lines are the Ling *et al.* solutions for $\langle c_1 \rangle$ and $\langle c_2 \rangle$. The black dashed line is the Ogata-Banks solution (53). Parameters are listed as SIM-05 to SIM-07 in Table I.

10 (see SIM-05 to SIM-07 listed in Table I). The results depicted in Fig. 8 were obtained for Pe $= 1$, 10, and 100. Solutions from the GITT (solid lines) and those from the solution of (24) and (25) (Ling *et al.* [36]) (dashed lines) are plotted. When Pe is high (i.e., Pe $= 100$), differences between the concentration solutions for the channel and the matrix are enhanced. The difference between the solutions obtained in the two regions decreases when the system becomes more diffusive (Pe $\to 0$). The results presented in Fig. 8 also show that the GITT results are in good agreement with the solution of Ling *et al.* [36] obtained for different different parameter pairs.

V. ANALYTICAL APPROXIMATION AND EFFECTIVE PARAMETERS

The semianalytical results obtained through the use of the GITT show that in some cases, the difference between the concentrations in the channel and in the matrix is very small [for instance, see Fig. 8(c)]. Inspection of Eqs. (24) and (25) suggests that, for any fixed λ and h (or, alternatively, Λ), $\langle c_1 \rangle \simeq \langle c_2 \rangle$ when Pe $\ll \epsilon^2$ for $\epsilon \to 0$ (i.e., $L \gg b$). In other words, the average concentration of the solute is similar in both the channel and the porous matrix under the appropriate dynamical conditions. Setting $\langle c_1 \rangle = \langle c_2 \rangle$ while using (24), one can derive the following approximate model formulation for the upscaled concentration in the channel:

$$\frac{\partial \langle c_1 \rangle}{\partial t} - (A_1 + A_3)\frac{\partial \langle c_1 \rangle}{\partial x} - A_2 \frac{\partial^2 \langle c_1 \rangle}{\partial x^2} = 0 \tag{52}$$

with continuous injection $\langle c_1 \rangle|_{x=0} = 1$. The formulation presented in Eq. (52) can be analytically solved following the procedure outlined in Ref. [58]. The Ogata-Banks solution [58] is valid for a continuous injection at the inlet of the channel with uniform flow and it admits the following

analytical solution:

$$\langle c_1 \rangle = \langle c_2 \rangle = \frac{1}{2}\left[\mathrm{erfc}\left(\frac{x - u_{\mathrm{eff}}t}{2\sqrt{D_{\mathrm{eff}}t}} \right) + \exp\left(\frac{u_{\mathrm{eff}}x}{D_{\mathrm{eff}}t} \right) \mathrm{erfc}\left(\frac{x + u_{\mathrm{eff}}t}{2\sqrt{D_{\mathrm{eff}}t}} \right) \right], \tag{53}$$

where the modified (i.e., effective) velocity and dispersion coefficients are defined as:

$$u_{\mathrm{eff}} = -(A_1 + A_3), \tag{54}$$

$$D_{\mathrm{eff}} = A_2. \tag{55}$$

It is important to note that the physical properties of the porous medium affect the transport in the channel since both u_{eff} and D_{eff} depend on λ and h. Although Eq. (53) is valid for continuous injection of an inert scalar, the one-dimensional ADE (52) can be solved for other types of boundary and initial conditions. Analytical solutions for Eq. (52) are available under more generic boundary and initial conditions through the use of the Unified Transform (also known as the Fokas method) [59]. Solutions can also be obtained by the well-known Duhamel theorem for an instantaneous pulse injection [60].

The results reported in Fig. 8 show that when $\langle c_1 \rangle \sim \langle c_2 \rangle$ (or $\mathrm{Pe} \ll \epsilon^2$), the solution (53), parameterized with u_{eff} (54) and D_{eff} (55), is in excellent agreement with the one obtained through the GITT. As a consequence, under the limiting condition $\epsilon \to 0$, the approximate formulation (52) can yield accurate predictions of the upscaled solute concentration while incorporating the parameters characterizing the porous matrix.

Such an approximation can largely reduce the computation time when estimating a large channel-matrix coupled system, however, when the matrix becomes more permeable: $\lambda \to 0$, solute is dispersed strongly within the porous matrix domain, which causes larger difference between the $\langle c_1 \rangle$ and $\langle c_2 \rangle$, and this further reduces the accuracy of the Ogata-Banks approximation.

To further investigate this, we plot three error maps: (1) the error between the GITT solution and the numerical solutions of (24) and (25) (Ling *et al.* [36]), (2) the error between the GITT solution and the 2D solution, and (3) the error between ADE solution and the numerical solutions of (24) and (25) (Ling *et al.* [36]). Figure 9 shows the error computed with Eq. (51) between the GITT solution and the numerical solutions of (24) and (25) (Ling *et al.* [36]) in a $\mathrm{Pe} - \lambda$ space, with the standard function f_{std} selected as the latter solution. Warmer colors indicate a larger error regions, and the dashed contours are 1%, 5% and 10% error bounds. Figure 10 shows the error computed with Eq. (51) between the GITT solution and the numerical solutions of the 2D problem [36]). From Fig. 10, it is apparent that the upscaled equation solved by the GITT has a wide range of accuracy in representing the 2D solution. Figure 11 shows the same error evaluation between the Ogata-Banks solution and the numerical solutions of (24) and (25) (Ling *et al.* [36]) in a $\mathrm{Pe} - \lambda$ space. For consistency, three error maps use the same color scale. We can see that the GITT has a good agreement with the numerical solution of the upscaled equation, and it suggests that the GITT algorithm is suitable for solving equations with the form of (24) and (25). Further, in Fig. 11, we can see the ADE solution has a reasonable accuracy, however, either a larger matrix permeability or a more advective transport can lead to low accuracy of the Ogata-Banks solution. Finally, a comparison between Fig. 9 and Fig. 11 shows that the Ogata-Banks solution has a smaller applicability zone than that of the GITT.

VI. SUMMARY AND CONCLUSIONS

Flow and transport in channel-matrix systems occur in a large variety of natural and industrial settings: Examples range from fractured geological formations to porous media-coated devices.

This paper investigates macroscopic transport of an inert scalar in a shear flow through an infinitely thin coupled channel-matrix system, which can be described by a system of coupled 1D partial differential equations. We develop a semianalytical solution based on the GITT. The GITT framework is applicable for any coupled system of one-dimensional partial differential equations
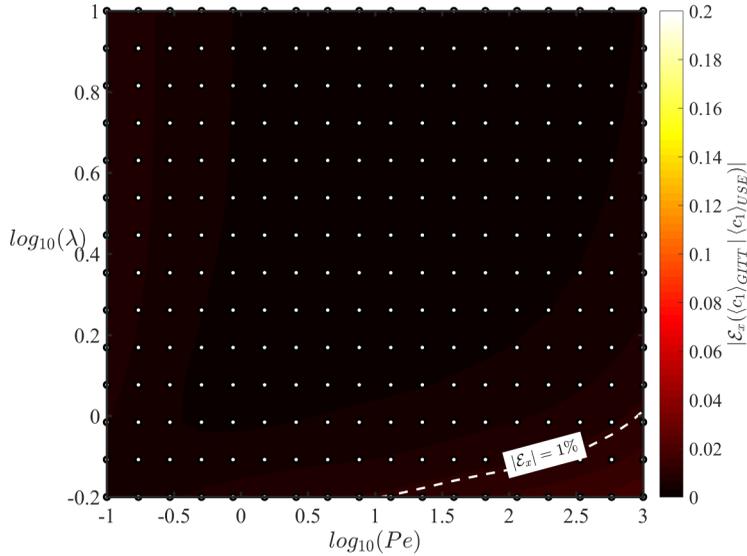
FIG. 9. Error between the GITT solution and the numerical solution of (24) and (25) (Ling *et al.* [36]). The white dots indicate where the error values are calculated exactly and the points in between are computed through linear interpolation. The dashed lines correspond to the 1%. The base of the logarithm in the figure is 10.

that is consistent with the general form analyzed in this work. The semianalytical solution consists of series summations, which are smooth and differentiable over the entire domain, and such solution form allows one to assess derived quantities, e.g., flux, transfer rate analytically.
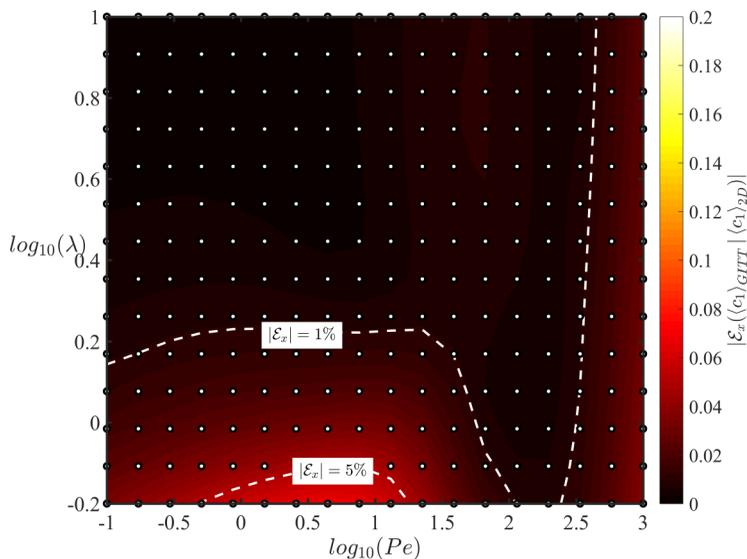

FIG. 10. Error between the GITT solution and the two-dimensional solution. The white dots indicate where the error values are calculated exactly and the points in between are computed through linear interpolation. The dashed lines correspond to the 1% and 5%. The base of the logarithm in the figure is 10.
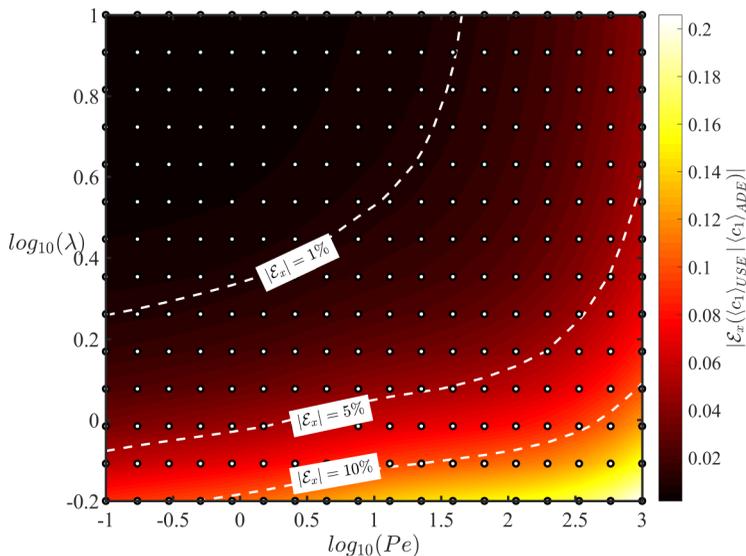
FIG. 11. Error between the Ogata-Banks solution (53) and the numerical solution of (24) and (25) (Ling *et al.* [36]). The white dots indicate where the error values are calculated exactly and the points in between are computed through linear interpolation. The dashed lines correspond to the 1%, 5%, and 10% error contours. The base of the logarithm in the figure is 10.

The GITT solver is implemented with Python and followed by a convergence study. The results show that, the GITT algorithm converges with large number of eigenfunctions (N) and small time step (δt). The solution is successfully compared with the spatially averaged numerical solution of the corresponding "microscale" 2D problem. The proposed integral transform solution is computationally efficient due to its analytical features. Finally, we show that under appropriate dynamic conditions, expressed in terms of Peclét number, the problem can be further simplified to a 1D partial differential equation (1D-PDE) for the average concentration in the channel and the matrix, which admits a closed-form analytical solution.

We show the accuracy of the various solutions through a parametric study in terms of the Peclét number and the geometric parameter λ. By evaluating the error between the GITT solution and the direct numerical solution of the upscaled equation, we validated the GITT. With comparison between the GITT solution and the 2D solution, we indicate that the GITT is expected to provide more accurate results when the matrix is less permeable and more diffusive. Further, the 1D-PDE representation provides high accuracy results when the solute flux between the channel and the matrix is irrelevant.

The error study can be used as a criterion for algorithm/model selection such that the most computationally efficient model can be used, without compromising prediction accuracy, depending on the specific values of relevant dimensionless numbers, that may vary across different applications. The flexibility of the proposed approach ensures the accuracy of the upscaled system, and at the same time, provides efficient estimation of solute migration in channel-matrix coupled systems.

Furthermore, the GITT algorithm can be applied to many other systems where the transport is modeled by coupled PDEs that have the general form shown in this study. The analytical series solution enables efficient estimation of higher derivative quantities such as the flux.

ACKNOWLEDGMENTS

APPENDIX

1. Upscaled equation

The upscaled equation derived in Ref. [36] writes:

$$\epsilon^2 \text{Pe} \frac{\partial \langle c_1 \rangle}{\partial t} + \epsilon^2 \text{Pe} \langle u_1 \rangle \frac{\partial \langle c_1 \rangle}{\partial x} = \epsilon^3 D_1^* \frac{\partial^2 \langle c_1 \rangle}{\partial x^2} - \phi \epsilon^2 \text{Pe} N_1 \frac{\partial \langle c_2 \rangle}{\partial x} - \phi \frac{3 D_{2,y}}{h} [\langle c_1 \rangle - \langle c_2 \rangle], \qquad (A1)$$

$$\epsilon^2 \text{Pe} \frac{\partial \langle c_2 \rangle}{\partial t} + \epsilon^2 \text{Pe} \langle u_2 \rangle \frac{\partial \langle c_2 \rangle}{\partial x} = \epsilon^3 D_2^* \frac{\partial^2 \langle c_2 \rangle}{\partial x^2} + \frac{M_I}{\phi h} \epsilon^2 \text{Pe} \frac{\partial \langle c_1 \rangle}{\partial x} + \frac{3}{\phi h} [\langle c_1 \rangle - \langle c_2 \rangle], \qquad (A2)$$

thus, we have:

$$A_1 = -\langle u_1 \rangle, \; A_2 = \frac{\epsilon D_1^*}{\text{Pe}}, \; A_3 = -\phi N_1, \; A_4 = -\frac{3 \phi D_{2,y}}{\epsilon^2 \text{Pe} h}, \; A_5 = \frac{3 \phi D_{2,y}}{\epsilon^2 \text{Pe} h}, \qquad (A3)$$

$$B_1 = -\langle u_2 \rangle, \; B_2 = \frac{\epsilon D_2^*}{\text{Pe}}, \; B_3 = -\frac{M_1}{\phi h}, \; B_4 = -\frac{3}{\epsilon^2 \text{Pe} \phi h}, \; B_5 = \frac{3}{\epsilon^2 \text{Pe} \phi h}, \qquad (A4)$$

where:

$$\langle u_1 \rangle = \frac{A}{2} + B + \frac{\Psi}{6}, \qquad (A5)$$

$$\langle u_2 \rangle = -\frac{\lambda E (e^{-h\lambda} - 1) - \lambda F (e^{h\lambda} - 1) + h \Psi}{h \lambda^2}, \qquad (A6)$$

and:

$$M_1 = -\frac{A}{2} - B - \frac{\Psi}{6}, \qquad (A7)$$

$$M_2 = \frac{5A}{24} + \frac{B}{3} + \frac{3\Psi}{40}, \qquad (A8)$$

$$N_1 = -\frac{h\Psi}{\lambda^2} - \frac{E e^{-h\lambda}}{\lambda} + \frac{F e^{h\lambda}}{\lambda}, \qquad (A9)$$

$$N_2 = \frac{e^{-h\lambda}[-2e^{h\lambda}(h^3 \lambda \Psi + 3E - 3F) - 3E(h^2 \lambda^2 - 2) + 3F e^{2h\lambda}(h^2 \lambda^2 - 2)]}{6 h \lambda^3}, \qquad (A10)$$

and:

$$I_f = \frac{7A^2}{240} + \frac{AB}{24} + \frac{A\Psi}{40} + \frac{7B\Psi}{360} + \frac{3\Psi^2}{560}, \qquad (A11)$$

$$\begin{aligned}
I_m = -\frac{e^{-2h\lambda}}{6h^2 \lambda^5} \{ & 3\lambda E^2 (h^2 \lambda^2 + e^{h\lambda}(h^2 \lambda^2 - 2h\lambda - 4)3h\lambda + e^{2h\lambda}(2 - h\lambda) + 2) \\
& - E e^{h\lambda} [3\lambda F (h^2 \lambda^2 + e^{2h\lambda}(h^2 \lambda^2 - 2h\lambda - 4) + e^{h\lambda}(6h^2 \lambda^2 + 8) + 2h\lambda - 4) \\
& - h\Psi(h^2 \lambda^2 + 2e^{h\lambda}(h^2 \lambda^2 - 3h\lambda + 3) - 6)] \\
& + F e^{2h\lambda} [3\lambda F (e^{h\lambda}(h^2 \lambda^2 + 2h\lambda - 4) + e^{2h\lambda}(h^2 \lambda^2 - 3h\lambda + 2) + h\lambda + 2) \\
& - h\Psi(2h^2 \lambda^2 + e^{h\lambda}(h^2 \lambda^2 - 6) + 6h\lambda + 6)] \},
\end{aligned} \qquad (A12)$$

$$D_1^* = D_f + \mathrm{Pe}^2 \frac{I_f}{D_f}, \tag{A13}$$

$$D_2^* = D_{2,x} + \mathrm{Pe}^2 \frac{I_m}{D_{2,y}}. \tag{A14}$$

2. Simulation parameters

All the parameters used in this study are listed in the following table.

TABLE I. Parameters used in the simulation.

	N	δt	Pe	ε	λ	h	ϕ	D_f	D_{mx}	D_{my}	Ψ
SIM-01	10	0.01	100	0.02	10	10	0.1	0.01	0.01	0.01	-1
SIM-02	50	0.01	100	0.02	10	10	0.1	0.01	0.01	0.01	-1
SIM-03	100	0.01	100	0.02	10	10	0.1	0.01	0.01	0.01	-1
SIM-04	200	0.01	100	0.02	10	10	0.1	0.01	0.01	0.01	-1
SIM-05	500	0.01	100	0.02	10	10	0.1	0.01	0.01	0.01	-1
SIM-06	500	0.01	10	0.02	10	10	0.1	0.01	0.01	0.01	-1
SIM-07	500	0.01	1	0.02	10	10	0.1	0.01	0.01	0.01	-1
SIM-08	500	0.01	100	0.02	1	10	0.1	0.01	0.01	0.01	-1
SIM-09	500	0.01	10	0.02	1	10	0.1	0.01	0.01	0.01	-1
SIM-10	500	0.01	1	0.02	1	10	0.1	0.01	0.01	0.01	-1
SIM-11	500	0.01	100	0.02	0.5	10	0.1	0.01	0.01	0.01	-1
SIM-12	500	0.01	10	0.02	0.5	10	0.1	0.01	0.01	0.01	-1
SIM-13	500	0.01	1	0.02	0.5	10	0.1	0.01	0.01	0.01	-1
SIM-14	500	0.05	100	0.02	10	10	0.1	0.01	0.01	0.01	-1
SIM-15	500	0.1	100	0.02	10	10	0.1	0.01	0.01	0.01	-1
SIM-16	500	0.5	100	0.02	10	10	0.1	0.01	0.01	0.01	-1
SIM-17	100	0.01	0.1	0.1	1	5	0.5	1	1	1	-0.1
SIM-18	100	0.01	10	0.1	10	5	0.5	1	1	1	-0.1
SIM-19	200	0.05	100	0.1	10	5	0.5	0.1	0.1	0.1	-0.1
SIM-20	200	0.05	10	0.1	10	5	0.5	0.1	0.1	0.1	-0.1
SIM-21	200	0.05	1	0.1	10	5	0.5	0.1	0.1	0.1	-0.1
SIM-22	1000	0.01	100	0.02	10	10	0.1	0.01	0.01	0.01	-1
SIM-23	2000	0.01	100	0.02	10	10	0.1	0.01	0.01	0.01	-1
SIM-24	5000	0.01	100	0.02	10	10	0.1	0.01	0.01	0.01	-1
SIM-25	500	0.005	100	0.02	10	10	0.1	0.01	0.01	0.01	-1
SIM-26	500	0.001	100	0.02	10	10	0.1	0.01	0.01	0.01	-1

[1] N. Tilton and L. Cortelezzi, Linear stability analysis of pressure driven flows in channels with porous walls, J. Fluid Mech. **604**, 411 (2008).

[2] I. Battiato, Self-similarity in coupled Brinkman/Navier-Stokes flows, J. Fluid Mech. **699**, 94 (2012).

[3] N. Tilton, E. Serre, D. Martinand, and R. M. Lueptow, A 3d pseudospectral algorithm for fluid flows with permeable walls: Application to filtration, Comput. Fluids **93**, 129 (2014).

[4] M. Ghisalberti, Obstructed shear flows: Similarities across systems and scales, J. Fluid Mech. **641**, 51 (2009).

[5] A. Papke and I. Battiato, A reduced complexity model for dynamic similarity in obstructed shear flows, Geophys. Res. Lett. **40**, 3888 (2013).

[6] D. Tang, E. Frind, and E. A. Sudicky, Contaminant transport in fractured porous media: Analytical solution for a single fracture, Water Resour. Res. **17**, 555 (1981).

[7] H. Rajaram and M. Arshadi, A similarity solution for reaction front propagation in a fracture–matrix system, Philos. Trans. R. Soc. A **374**, 20150424 (2016).

[8] H. Marschner and B. Dell, Nutrient uptake in mycorrhizal symbiosis, Plant Soil **159**, 89 (1994).

[9] B.-Y. Cao, M. Chen, and Z.-Y. Guo, Liquid flow in surface-nanostructured channels studied by molecular dynamics simulation, Phys. Rev. E **74**, 066311 (2006).

[10] G. D. Bixler and B. Bhushan, Bioinspired rice leaf and butterfly wing surface structures combining shark skin and lotus effects, Soft Matter **8**, 11271 (2012).

[11] C. Deck, C. Ni, K. Vecchio, and P. Bandaru, The response of carbon nanotube ensembles to fluid flow: Applications to mechanical property measurement and diagnostics, J. Appl. Phys. **106**, 074304 (2009).

[12] A. Konings, G. Katul, and S. Thompson, A phenomenological model for the flow resistance over submerged vegetation, Water Resour. Res. **48**, 2 (2012).

[13] I. Battiato and S. Rubol, Single-parameter model of vegetated aquatic flows, Water Resour. Res. **50**, 6358 (2014).

[14] S. Rubol, I. Battiato, and F. P. J. de Barros, Vertical dispersion in vegetated shear flows, Water Resour. Res. **52**, 8066 (2016).

[15] S. Rubol, B. Ling, and I. Battiato, Universal scaling-law for flow resistance over canopies with complex morphology, Sci. Rep. **8**, 4430 (2018).

[16] R. J. Lowe, U. Shavit, J. L. Falter, J. R. Koseff, and S. G. Monismith, Modeling flow in coral communities with and without waves: A synthesis of porous media and canopy flow approaches, Limnol. Oceanogr. **53**, 2668 (2008).

[17] L. Wang, D. Li, Z. Gao, T. Sun, X. Guo, and E. Bou-Zeid, Turbulent transport of momentum and scalars above an urban canopy, Bound. Layer Meteorol. **150**, 485 (2014).

[18] Y. Méheust and J. Schmittbuhl, Flow enhancement of a rough fracture, Geophys. Res. Lett. **27**, 2989 (2000).

[19] D. Poggi, G. Katul, and J. Albertson, A note on the contribution of dispersive fluxes to momentum transfer within canopies, Bound. Layer Meteorol. **111**, 615 (2004).

[20] W. P. Breugem, B. J. Boersma, and R. E. Uittenbogaard, The influence of wall permeability on turbulent channel flow, J. Fluid Mech. **562**, 35 (2006).

[21] S. C. Hirata, B. Goyeau, and D. Gobin, Stability of natural convection in superposed fluid and porous layers: Influence of the interfacial jump boundary condition, Phys. Fluids **19**, 058102 (2007).

[22] S. Mahjoob and K. Vafai, A synthesis of fluid and thermal transport models for metal foam heat exchangers, Int. J. Heat Mass Transf. **51**, 3701 (2008).

[23] C. Manes, D. Pokrajac, I. McEwan, and V. Nikora, Turbulence structure of open channel flows over permeable and impermeable beds: A comparative study, Phys. Fluids **21**, 125109 (2009).

[24] C. Manes, D. Poggi, and L. Ridolfi, Turbulent boundary layers over permeable walls: Scaling and near wall structure, J. Fluid Mech. **687**, 141 (2011).

[25] B. Ling and I. Battiato, Rough or wiggly? Membrane topology and morphology for fouling control, J. Fluid Mech. **862**, 753 (2019).

[26] Z. Zhou, B. Ling, I. Battiato, S. M. Husson, and D. A. Ladner, Concentration polarization over reverse osmosis membranes with engineered surface features, J. Membr. Sci. **617**, 118199 (2021).

[27] A. L. McGaughey, P. Karandikar, M. Gupta, and A. E. Childress, Hydrophobicity versus pore size: Polymer coatings to improve membrane wetting resistance for membrane distillation, ACS Appl. Polym. Mater. **2**, 1256 (2020).

[28] A. Fischer, K. Pettigrew, D. Rolison, R. Stroud, and J. Long, Incorporation of homogeneous, nanoscale mno2 within ultraporous carbon structures via self-limiting electroless deposition: Implications for electrochemical capacitors, Nano Lett. **7**, 281 (2007).

[29] O. Alifanov, V. Cherepanov, and A. Morzhukhina, Mathematical modeling of ultraporous nonmetallic reticulated materials, J. Eng. Phys. Thermophys. **88**, 124 (2015).

[30] B. Ling, M. Oostrom, A. M. Tartakovsky, and I. Battiato, Hydrodynamic dispersion in thin channels with micro-structured porous walls, Phys. Fluids **30**, 076601 (2018).

[31] I. Battiato, Effective medium theory for drag-reducing micro-patterned surfaces in turbulent flows, Eur. Phys. J. E **37**, 19 (2014).

[32] I. Battiato, P. Bandaru, and D. M. Tartakovsky, Elastic Response of Carbon Nanotube Forests to Aerodynamic Stresses, Phys. Rev. Lett. **105**, 144504 (2010).

[33] L. Salerno, G. Cardillo, and C. Camporeale, Aris-taylor dispersion in the subarachnoid space, Phys. Rev. Fluids **5**, 043102 (2020).

[34] H. Guo, H. Zhu, and S. Veerapaneni, Simulating cilia-driven mixing and transport in complex geometries, Phys. Rev. Fluids **5**, 053103 (2020).

[35] Y. Sun, P. Sanaei, L. Kondic, and L. J. Cummings, Modeling and design optimization for pleated membrane filters, Phys. Rev. Fluids **5**, 044306 (2020).

[36] B. Ling, A. M. Tartakovsky, and I. Battiato, Dispersion controlled by permeable surfaces: Surface properties and scaling, J. Fluid Mech. **801**, 13 (2016).

[37] M. Dejam, H. Hassanzadeh, and Z. Chen, Shear dispersion in a fracture with porous walls, Adv. Water Resour. **74**, 14 (2014).

[38] R. M. Cotta, K. M. Lisboa, and J. L. Z. Zotin, Integral transforms for flow and transport in discrete and continuum models of fractured heterogeneous porous media, Adv. Water Resour. **142**, 103621 (2020).

[39] M. Dejam, Advective-diffusive-reactive solute transport due to non-newtonian fluid flows in a fracture surrounded by a tight porous medium, Int. J. Heat Mass Transf. **128**, 1307 (2019).

[40] M. Dejam, Dispersion in non-newtonian fluid flows in a conduit with porous walls, Chem. Eng. Sci. **189**, 296 (2018).

[41] J. M. Nordbotten, M. A. Celia, S. Bachu, and H. K. Dahle, Semianalytical solution for co2 leakage through an abandoned well, Environ. Sci. Technol. **39**, 602 (2005).

[42] H. B. Fischer, *Mixing in Inland and Coastal Waters* (Academic Press, New York, 1979).

[43] F. P. J. de Barros, W. B. Mills, and R. M. Cotta, Integral transform solution of a two-dimensional model for contaminant dispersion in rivers and channels with spatially variable coefficients, Environ. Modell. Softw. **21**, 699 (2006).

[44] F. P. J. de Barros and A. Fiori, First-order based cumulative distribution function for solute concentration in heterogeneous aquifers: Theoretical analysis and implications for human health risk assessment, Water Resour. Res. **50**, 4018 (2014).

[45] D. Roubinet, J.-R. de Dreuzy, and D. M. Tartakovsky, Semi-analytical solutions for solute transport and exchange in fractured porous media, Water Resour. Res. **48**, W01542 (2012).

[46] E. Perucca, C. Camporeale, and L. Ridolfi, Estimation of the dispersion coefficient in rivers with riparian vegetation, Adv. Water Resour. **32**, 78 (2009).

[47] T. Musner, A. Bottacin-Busolin, M. Zaramella, and A. Marion, A contaminant transport model for wetlands accounting for distinct residence time bimodality, J. Hydrol. **515**, 237 (2014).

[48] N. Ahmad, A. Wörman, A. Bottacin-Busolin, and X. Sanchez-Vila, Reactive transport modeling of leaking co 2-saturated brine along a fractured pathway, Int. J. Greenhouse Gas Contr. **42**, 672 (2015).

[49] M. N. Özişik, and M. D. Mikhailov, *Unified Analysis and Solutions of Heat and Mass Diffusion* (Dover, London, 1994).

[50] R. M. Cotta, *Integral Transforms in Computational Heat and Fluid Flow* (CRC Press, Boca Raton, FL, 1993).

[51] K. Malek and M.-O. Coppens, Knudsen self-and fickian diffusion in rough nanoporous media, J. Chem. Phys. **119**, 2801 (2003).

[52] R. Cotta, M. Ungs, and M. Mikhailov, Contaminant transport in finite fractured porous medium: Integral transforms and lumped-differential formulations, Ann. Nucl. Energy **30**, 261 (2003).

[53] C. Chen and H. Qin, A mathematical modeling of the reverse osmosis concentration process of a glucose solution, Processes **7**, 271 (2019).

[54] M. Van Genuchten and P. Wierenga, Mass transfer studies in sorbing porous media I. Analytical solutions, Soil Sci. Soc. Am. J. **40**, 473 (1976).

[55] L. Sphaier, R. Cotta, C. Naveira-Cotta, and J. Quaresma, The unit algorithm for solving one-dimensional convection-diffusion problems via integral transforms, Int. Commun. Heat Mass Transf. **38**, 565 (2011).

[56] R. M. Cotta, D. C. Knupp, C. P. Naveira-Cotta, L. A. Sphaier, and J. N. Quaresma, Unified integral transforms algorithm for solving multidimensional nonlinear convection-diffusion problems, Numer. Heat Transf. A **63**, 840 (2013).

[57] F. P. J. de Barros and R. M. Cotta, Integral transforms for three-dimensional steady turbulent dispersion in rivers and channels, Appl. Math. Model. **31**, 2719 (2007).

[58] A. Ogata and R. B. Banks, *A Solution of the Differential Equation of Longitudinal Dispersion in Porous Media: Fluid Movement in Earth Materials* (US Government Printing Office, Washington, DC, 1961).

[59] F. P. J. de Barros, M. J. Colbrook, and A. S. Fokas, A hybrid analytical-numerical method for solving advection-dispersion problems on a half-line, Int. J. Heat Mass Transf. **139**, 482 (2019).

[60] J. P. Guerrero, E. Pontedeiro, M. T. van Genuchten, and T. Skaggs, Analytical solutions of the one-dimensional advection–dispersion solute transport equation subject to time-dependent boundary conditions, Chem. Eng. J. **221**, 487 (2013).